LAWRENCE
LIVERMORE
NATIONAL
LABORATORY

UCRL-PROC-221531

Tomographic wavefront correction for the LSST

D. W Phillion, S. S. Olivier, K. Baker, L. Seppala, S. Hvisc

May 22, 2006

Astronomical Telescopes and Instrumentation 2006 SPIE Conference
Orlando, FL, United States
May 24, 2006 through May 31, 2006

Updated October 14, 2003

†Tomographic wavefront correction for the LSST

Donald W. Phillion[a], Scot S. Olivier[a], Kevin Baker[a], Lynn Seppala[a], Stacie Hvisc[a, b]
[a]Lawrence Livermore National Laboratory, [b]University of Arizona

ABSTRACT

The Large Synoptic Survey Telescope (LSST) is a three mirror modified Paul-Baker design with an 8.4m primary, a 3.4m secondary, and a 5.0m tertiary followed by a 3-element refractive corrector producing a 3.5 degree field of view. This design produces image diameters of <0.3 arcsecond 80% encircled energy over its full field of view. The image quality of this design is sufficient to ensure that the final images produced by the telescope will be limited by the atmospheric seeing at an excellent astronomical site. In order to maintain this image quality, the deformations and rigid body motions of the three large mirrors must be actively controlled to minimize optical aberrations. By measuring the optical wavefront produced by the telescope at multiple points in the field, mirror deformations and rigid body motions that produce a good optical wavefront across the entire field may be determined. We will describe the details of the techniques for obtaining these solutions. We will show that, for the expected mirror deformations and rigid body misalignments, the solutions that are found using these techniques produce an image quality over the field that is close to optimal. We will discuss how many wavefront sensors are needed and the tradeoffs between the number of wavefront sensors, their layout and noise sensitivity.

Keywords: active optics, tomographic wavefront correction, LSST, Large Synoptic Survey Telescope

1. INTRODUCTION

The Large Synoptic Survey Telescope (LSST) is a three mirror telescope design[1, 2, 3] with three fused silica corrector lenses and a fused silica filter that is designed to produce images across its entire 3.5 degree diameter field that are many times smaller than expected from atmospheric turbulence in good seeing conditions at the best sites for ground-based optical astronomical observatories. The silicon CCD will be about 630 mm across with 10 μm square pixels and have more than three billion pixels. The CCD will actually be actually a mosaic of 12x12 cm rafts, each consisting of a 3x3 square array of 4x4 cm chips. It will map most of the sky every several nights in a series of 15 second exposures. Six filters will cover the spectrum from the near ultraviolet to the near infrared, although not at once. The lenses, filter, and CCD comprise an assembly that will be moved slightly as a unit in z whenever the filter is switched. The science[4] that will be carried out by the LSST telescope's includes mapping the distribution of dark matter and dark energy using weak gravitational lensing, supernova cosmology, and detection of new objects in the solar system. The tremendous amount of data that is collected will be archived and will be able to be accessed by anybody in the world.

This design produces image diameters of <0.3 arcsecond 80% encircled energy over its full field of view for no atmosphere. In order to maintain this image quality, the deformations and rigid body motions of the three large mirrors must be actively controlled[5] to minimize optical aberrations. This active control consists both of changing the mirror shapes with actuators and also of moving the mirrors with all degrees of freedom except for the degenerate rotations about the optical axis. Since the primary and tertiary mirrors are fabricated from a single monolithic piece of glass, they cannot move independently. They also must bend together in the sense that there is one set of deformations that is applied to the monolithic primary-tertiary mirror.

We show that with reasonable initial mirror deformations and rigid body motions, that by measuring the wavefront at four or more positions about the circumference, that mirror deformations and rigid body motions may be computed and made that produce nearly the ideal image quality across the entire field.

We use least squares singular value decomposition (SVD) [6, 7, 8]. It is important to realize that the solution that is found is not the ideal baseline design and may not even be any closer to the ideal baseline design than was the initial optical system state, but this does not matter: What is important is that good image quality be obtained across the entire field. It is also important that this solution be stable with repeated iterations and not walk off. We have always found that after one or two iterations the solution is absolutely stable and unchanging in the absence of noise unless the SVD maximum condition value is chosen to be excessively large. Even with wavefront sensor noise, we have found that the solution is stable in the sense that there is no walk-off, just jitter about a point in the solution space. We have added a penalty term for walk-off to the least squares SVD algorithm but have never found it necessary to use it.

The least squares SVD solution method treats the optical system as a linear system: the inputs are the mirror deformations and rigid body motions and the outputs are the wavefront sensor measurements. The problem is made discrete and finite by working with a finite set of modes for the mirror deformations and by representing the wavefront sensor wavefronts by finite modal expansions. The inputs that can be changed are called controllables and the outputs that can be measured are called observables. For instance, not just the pistons but also the tilts for the wavefront sensor wavefronts are unobservables. This is because the positions of the guide stars used by the wavefront sensors will either not be known sufficiently accurately or not be known at all. Consequently, distortion of the field cannot be observed and corrected.

Because the system is not linear, the solution that is found is not ideal, but the closer the initial state is to the ideal baseline design, the better the solution is that is found. The key to understanding what is happening is to realize that there are output states that cannot be achieved by any input state in the linear model that is used by the least squares SVD algorithm. The SVD least squares algorithm tries to achieve the null vector in the output space (except when there is a penalty term for walk-off). When the output is in a state that is orthogonal to the image of the input space, the least squares SVD algorithm will not be able to do any better. Such an output state is possible because the system is nonlinear. The further away the initial state is from the ideal baseline design, the greater in magnitude is the component of the corresponding output state that is orthogonal to the image of the input space. Output modes which are orthogonal to the image of the controllable space are uncontrollable.

The starting point for the least squares SVD algorithm is to compute the sensitivity matrices relating the wavefront sensor wavefronts to the mirror deformations and rigid body motions. There will be as many sensitivity matrices as there are wavefront sensors to be fitted. We do this entirely by ray tracing. There is an alternative way using Zernike transformation matrices to obtain that part of the sensitivity matrices that is due to the mirror deformations. Although we do not discuss this alternative way in this paper because it is not sufficiently precise, we did implement this method and use it as a check against the ray tracing method. The reason that it is inexact even perturbatively is that the secondary and tertiary mirrors are not in planes that are conjugate to the primary mirror, so one can't simply add the phase perturbations. The transformation matrices arise because off-axis field points have off-center footprints on the secondary and tertiary mirrors and because a Zernike function in one coordinate system can be expanded in terms of Zernike functions in a different coordinate system having a different origin and different normalizing pupil radius. There is a certain ordering of Zernike functions which groups Zernike functions into shells having the property that Zernike functions in one coordinate system can be expressed in terms of Zernike functions in another coordinate system having the same and lower shell numbers. In addition to ray tracing being the correct and accurate way to compute the sensitivity matrices, it also makes it straightforward to use whatever set of modes we wish for the mirror deformations and to use whatever set of modes we wish for the wavefront sensor wavefront modal expansions. Furthermore, these two sets of modes do not have to be same. For instance, we have added cone modes to the set of mirror deformation functions.

Earlier work using SVD least squares for the LSST tomographic wavefront correction was done by Regis Tessieres and James H Burge[7]. Our work is much more comprehensive and uses ray tracing for everything rather than using the Zernike transformation matrices to compute that part of the sensitivity matrices due to the mirror deformations. Their work uses tables of Zernike transformation formulas. (The Zernike transformation matrices can also be worked out

using recursion relations, which we wrote into the program). Our LSST tomographic wavefront correction model is implemented in the stand alone *Telescope AO* code which runs on Windows XP Professional and which can be obtained from the authors[9].

2. RAY TRACING

Both the sensitivity matrices and the wavefront sensor wavefronts are computed by ray tracing. Considerable care is required in doing this. First the reference wavefront sensor wavefronts are computed. This is done by tracing a parallel bundle of rays for each field point for the ideal baseline design. For each ray bundle, its cluster point in image space is computed. This is defined as that location where the rms spot radius is smallest. The far field wavefronts are then computed about the cluster points. This means finding where the image space rays intersect a sphere of very large radius centered on the cluster point. All the opl's to this sphere are then incremented by the radius of the sphere. This is done in the limit of a sphere of infinite radius. For a sphere of very large radius, the interceptions are of course virtual and the opl's to the sphere are of course negative. Remember that the image space conceptually is infinite in all directions even though in reality there is a corrector lens very close to the CCD. To compute the sensitivity matrices, one perturbation at a time is applied to the optical system. The parallel ray bundles are then ray traced, their cluster points found, and the wavefronts about those cluster points computed. The corresponding reference wavefronts are then subtracted. But these cluster points are displaced from the positions of the corresponding reference cluster points. These displacements give rise to corrections to the tilt and focus terms. These computations are discussed in appendices A and B and require the ABCD ray matrix for the telescope. When computing the sensitivity matrices using ray tracing, the individual perturbations must be finite. The size of the perturbations must be chosen sufficiently large so as to make numerical errors fractionally small for the changes from the reference quantities and yet must at the same time be chosen sufficiently small so as to still be perturbations. Also, the sensitivity matrices work in terms of normalized quantities. The normalizations are chosen so that unit values correspond to representative perturbations that might be expected for the initial state. The wavefront sensor error wavefronts are actually the changes in the wavefronts from the reference wavefronts. For the real telescope, the actual measured wavefronts for the wavefront sensors will likewise be corrected for what the reference wavefront sensor wavefronts are computed to be.

3. SVD LEAST SQUARES ALGORITHM

The SVD least squares algorithm[5, 6, 7] finds mirror deformations and rigid body motions which give wavefront sensor wavefronts that match as closely as possible in a least squares sense the wavefront sensor error wavefronts. Recall that the wavefront sensor error wavefronts are the measured wavefront sensor wavefronts minus the computed reference wavefront sensor wavefronts. The negative of these mirror deformations and rigid body motions are then applied to the optical system. Define

$$\mathbf{C}_{goal}\left(\Omega_j\right)=\begin{bmatrix} a^{(\Omega_j)}(0) \\ \vdots \end{bmatrix} \tag{1}$$

to be the wavefront sensor error wavefronts for the field directions Ω_j. These are assumed to be related to the mirror deformations and rigid body motions by the linear model:

$$\begin{bmatrix} a^{(\Omega_j)}(0) \\ \vdots \end{bmatrix}=\begin{bmatrix} \mathbf{M}_1\left(\Omega_j\right) & \mathbf{M}_2\left(\Omega_j\right) \end{bmatrix}\begin{bmatrix} \mathbf{B}_1 \\ \mathbf{B}_2 \end{bmatrix} \tag{2}$$

Zernikecoefficients for wavefront sensor at Ω_j field angle

sensitivity matrix for mirror deformations

sensitivity matrix for mirror rigid body motions

mirror deformations and rigid body

For definiteness, we assume that the mirror deformations and wavefront sensor wavefronts are represented by Zernike functions, but this does not have to be the case. We will first present the theory without the penalty term for walk-off and then show how this term is added to the formalism. Least squares SVD finds the solution vector B which minimizes the sum:

$$\sum_j \left[\mathbf{C}_{goal}\left(\Omega_j\right) - \mathbf{M}\left(\Omega_j\right)\mathbf{B} \right]^T \mathbf{W}_1 \left[\mathbf{C}_{goal}\left(\Omega_j\right) - \mathbf{M}\left(\Omega_j\right)\mathbf{B} \right] \tag{3}$$

Here W_1 is a diagonal weighting matrix with 1's for observable modes and 0's for unobservable modes, which will usually be wavefront sensor piston and tilts. It has a subscript 1 in order to distinguish it from a second weighting matrix which we will be defining shortly. For inputs which are not to be controlled, we set the corresponding columns in the M matrices to zero. Minimization gives the equation:

$$\mathbf{A}\,\mathbf{B} = \mathbf{C} \tag{4a}$$

where

$$\mathbf{A} = \sum_j \mathbf{M}\left(\Omega_j\right)^T \mathbf{W}_1 \mathbf{M}\left(\Omega_j\right) \tag{4b}$$

and

$$\mathbf{C} = \sum_j \mathbf{M}\left(\Omega_j\right)^T \mathbf{W}_1 \mathbf{C}_{goal}\left(\Omega_j\right) \tag{4c}$$

The matrix **A** is real symmetric. Singular value decomposition represents **A** in the form

$$\mathbf{A} = \mathbf{U}\,\mathbf{D}\,\mathbf{V}^T \tag{5}$$

where **U** and **V** are real orthogonal matrices and **D** is a diagonal non-negative matrix. **D** has the singular values as its diagonal elements, arranged from the largest to the smallest. If **A** is singular, then at least one of its SVD singular values will be zero. For us, the matrix **A** will always be completely singular, but this is no problem for finding the pseudo-inverse using singular value decomposition. If none of the singular values were zero or extremely small compared to the other singular values, the inverse would be

$$\mathbf{A}^{-1} = \mathbf{V}\,\mathbf{D}^{-1}\,\mathbf{U}^T \tag{6}$$

An important parameter in SVD is the maximum condition factor. For singular values that are zero or which are smaller than the largest singular value by a factor greater than the maximum condition factor, the corresponding diagonal element in $\mathbf{D}^{-1}$ is made zero. Then $\mathbf{A}^{-1}$ is a pseudo-inverse, not the actual inverse, which does not exist.

The penalty term for walk-off from the home position may now be easily added to the formalism. The home position is the configuration at iteration zero, not the baseline design. After all, for the real telescope the actuator positions that give the baseline design will not be known. Let $\mathbf{B}_0$ be the accumulated changes from the home position at iteration zero. Since the **B** vector represents changes, the walk-off penalty term should be a positive semi-definite quadratic form in $\mathbf{B}+\mathbf{B}_0$:

$$\left(\mathbf{B}+\mathbf{B}_0\right)^T \mathbf{W}_2 \left(\mathbf{B}+\mathbf{B}_0\right) \tag{7}$$

This should be added with some multiplier λ to the sum to be minimized. Minimization then gives the equation:

$$\left(\mathbf{A}+\lambda\,\mathbf{W}_2\right)\mathbf{B} = \mathbf{C} - \lambda\,\mathbf{W}_2\,\mathbf{B}_0 \tag{8}$$

4. SIMULATIONS

Everything was done by ray tracing: This includes both the computation of the sensitivity matrices for the wavefront sensors and the computation of the wavefronts for the wavefront sensors for the mirror deformations and rigid body motions at each iteration. The ray tracing was always done with a square grid of rays covering the primary mirror aperture. Only those rays making it through the optical system without vignetting were kept. In addition to the wavefronts sensors used in the fitting by the SVD least squares algorithm, there was always a set of non-fitted wavefront sensors which covered the field that was used to verify that that the solution gave good image quality over the entire

field, not just at the locations of the fitted wavefront sensors. Most of the simulations have the fitted wavefront sensors only on the circumference. One of our findings is that having all the fitted wavefront sensors uniformly spaced about the circumference rather than having some of them in the interior always works at least almost as well and sometimes works even better. Therefore there is no requirement for having wavefront sensors in the interior of the field.

We represent the deformations on the mirrors by Zernike functions. The simulations have been carried out with 9, 16, 25, and 36 Zernike functions. Our Zernike function ordering convention organizes the Zernike functions into shells. The number of Zernike functions in shells 0 through n_{shell}, inclusive, is $(n_{shell} + 1)^2$. However, the model has the flexibility to use any set of Zernike functions, not just the first $(n_{shell} + 1)^2$ for some n_{shell}, Also, actual bending modes for the real mirrors can be straightforwardly added to the model. This has already been done for the cone modes, but the cone modes were not used for any of simulation studies presented here. The model also has the capability to put higher order uncorrected deformations on the mirrors, although, again, we did not do this in any of the simulation results presented in this paper.

The simulations were done with different wavefront sensor configurations, different atmospheric seeing conditions, and different numbers of Zernike functions. In order to allow comparison, the initial deformations and rigid body motions for the optical system were always the same. These deformations and rigid body motions are specified by equations which can be edited and saved to or read from a text file. These equations can and do include random variables. The initial mirror deformations are given by a randomly signed 0.05 $N^{-1.25}$ spectrum for $N \geq 3$, giving the coefficients in millimeters for focus and above for the unnormalized Zernike functions. Since the same random number seed was always used, the same sequence was always generated. This represents 9 μm rms of deformation over a circular aperture. The primary and tertiary mirrors always bend together, so the bending is specified for the primary-tertiary monolithic mirror, rather than independently for the primary and tertiary mirrors. The rigid body translational motions were chosen to be uniformly distributed random variables over the interval [-1, +1] millimeters and the rigid body tilts were chosen to be uniformly distributed random variables over the interval $[-10^{-4}, +10^{-4}]$ radians. Again, since the same random number generator seed was always used, the same rigid body motions were always generated. Since the primary and tertiary move together, rigid body motions are only specified for the primary-tertiary monolithic mirror, not individually for the primary and tertiary mirrors.

All the simulations were done at the center wavelength of 777.5 nm in the I band. However, the model permits one to choose whichever band and whatever wavelength one wishes. The atmospheric turbulence was assumed to be at a height of 500 meters and was assumed to be frozen and carried by a 3 meter/second wind. The integration time was 15 seconds. Only the atmospheric turbulence contributed to the wavefront sensor errors. The reason for this restriction in the study of wavefront sensor error sources is that we realized that if 100 square arc-minutes were available for each wavefront sensor, then the probability of finding a star bright enough for photon noise and read noise errors to be negligible was essentially 100%. The Fried coherence length r0 at λ=500 nm was varied between 0.75 meters and 0.025 meters. For seeing condition worse than r0=0.1 meters at λ=500 nm, observations probably would not be made at all.

For the wavefront sensors on the circumference, square and hexagonal configurations were studied. Figure 1 shows one possible scenario for the CCD rafts[10] which allows for four large area wavefront sensors on a square on the circumference that are just inside the 3.5 degree diameter field of view. These areas will be used either for a Shack-Hartmann sensor which can be moved within the area or by a curvature wavefront sensor.

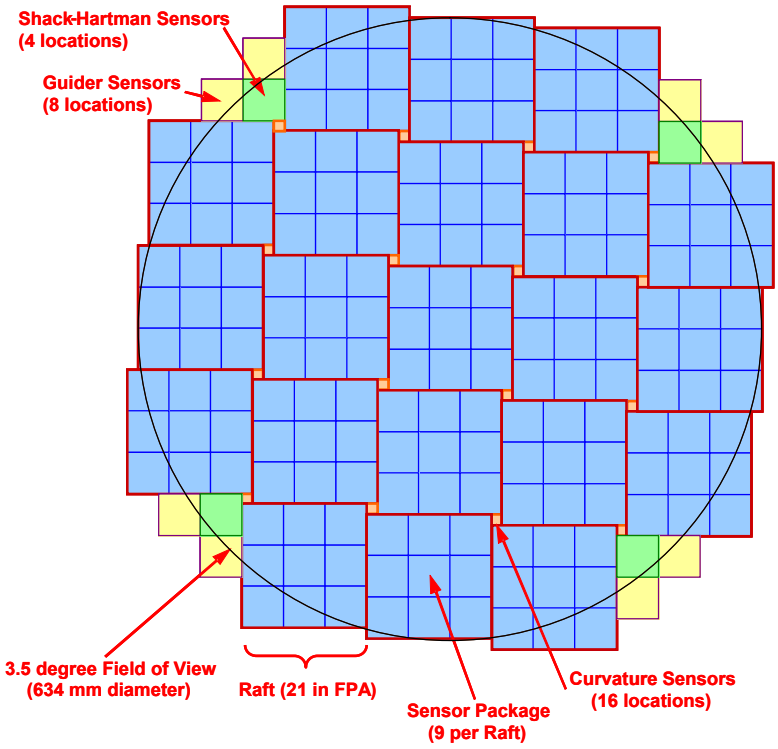

FIGURE 1

Possible LSST CCD configuration. There are twenty-one 12x12 cm rafts, each made up of a 3x3 array of 4x4 cm chips. The pixel size is 10 μm square, giving a total of 3,024,000,000 pixels. Each CCD pixel is 0.2 arc seconds on the sky. There are four large areas on the corners of a square about the circumference just inside the field of view. Each has more than one hundred square arc minutes of area for use by a wavefront sensor. The rafts are staggered so as to create 16 smaller 1x1 cm areas for use by curvature wavefront sensors.

There are also sixteen 1x1 cm interior areas on a 4x4 grid. The outer twelve are designated for use by curvature wavefront sensors. It is possible that these areas will be increased in size to 1.5x1.5 cm. It is also possible that these areas will simply be eliminated. The wavefront sensor configurations which were studied were a square on the 3.5 degree diameter circumference, a hexagon on the 3.5 degree diameter circumference, and the outer twelve for the cases of either all twelve being present or either 1, 3, 5, or 7 at a corner being missing. The probability of finding a star bright enough to use for curvature sensing is only about 50% for these small 10 square arc minute areas.

If tilts are not measured, then in general four wavefront sensors are required to ensure that the imaging is good across the entire field, not just at the wavefront sensor positions. If only nine Zernike functions are used, then three wavefront sensors suffice. For sixteen, twenty-five, and thirty-six Zernike functions, four wavefront sensors are required to ensure that good imaging at the wavefront sensor positions ensures good imaging across the entire field. If the guide star locations were known sufficiently accurately for the tilt measurements to be accurate, then five wavefront sensors would be required to ensure that good imaging and small distortion at the wavefront sensor positions guaranteed good imaging and small distortion across the entire field. These cases were studied versus seeing conditions for nine, sixreen, twenty-five, and thirty-six Zernike functions. The rms spot radii are always after two iterations. Further iterations result in almost no changes in the solutions. Note that the rms spot radii are for the telescope with no atmosphere. The way the atmosphere is affecting the rms spot radii is by adding errors to the wavefront sensors. Once a telescope solution is found, the rms spot radii are computed for the solution with no atmosphere. This is what is desired. We wish to show that these rms spot radii are still many times smaller than what be produced by the atmospheric turbulence for a telescope having perfect imaging.

Figures 2 shows how a square and hexagon wavefront sensor configuration on the boundary perform versus atmospheric seeing conditions. Figure 2 also compares the performance with nine, sixteen, twenty-five, and thirty-six Zernike functions. Figure 4 shows how the exterior box of twelve wavefront sensors performs versus atmospheric seeing conditions. This figure also shows how the performance is degraded by having 3, 5, or 7 wavefront sensors at a corner omitted. Having all the omitted wavefront sensors be in one corner presumably gives the worst performance. We find that the four wavefront sensors on the 3.5 degree circumference perform about the same as having all twelve wavefront sensors on the outer box for the small interior areas. And having a hexagon on the circumference works best.

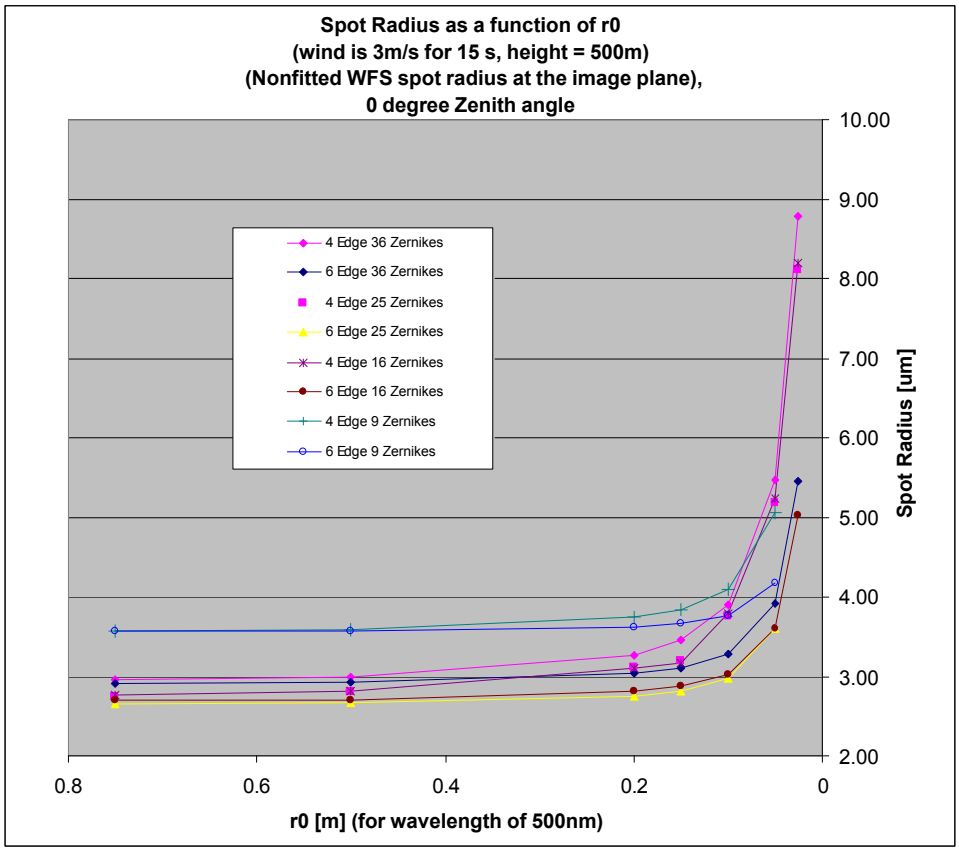

FIGURE 2

Rms spot radius versus atmospheric seeing for the tomographically corrected telescope after two iterations. A "bright" star is assumed. The turbulence is at 500 meters altitude, there is a wind of 3 meters/second, the integration time is 15 seconds, and the zenith angle is 0°. The Fried r_0 values are at λ=500 nm. The wavefront sensor configuration was either a square ("4 Edge") or a hexagon ("6 Edge") on the 3.5 degree diameter field circumference.

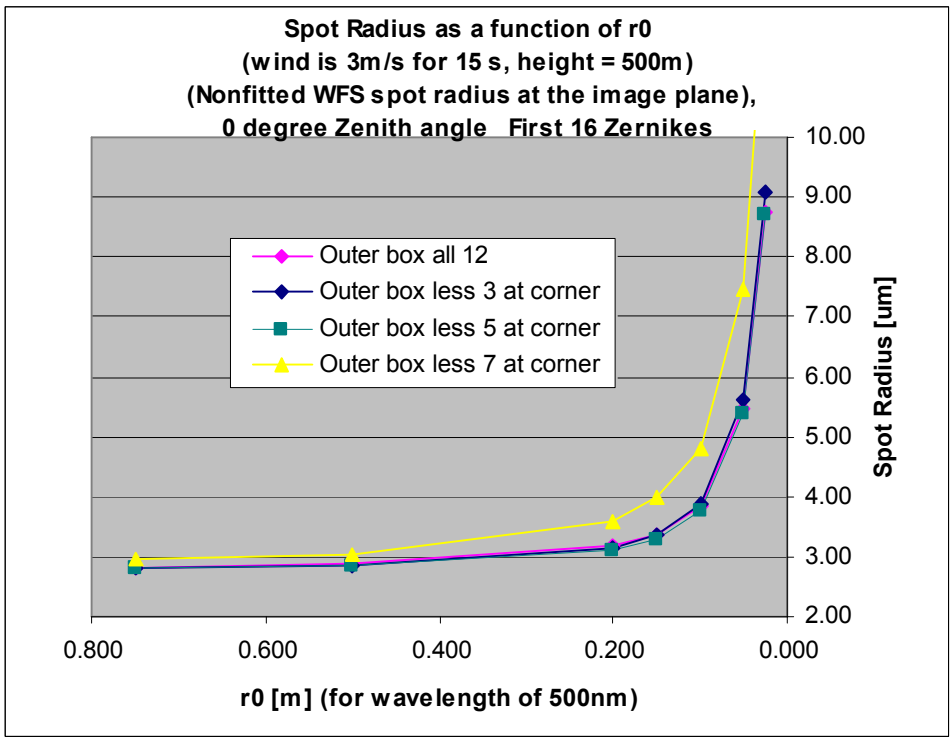

FIGURE 3

Rms spot radius versus atmospheric seeing for the tomographically corrected telescope after two iterations. A "bright" star is assumed. The turbulence is at 500 meters altitude, there is a wind of 3 meters/second, the integration time is 15 seconds, and the zenith angle is 0°. The Fried r_0 values are at λ=500 nm. The wavefront sensor configurations are the outer of box of twelve shown in Figure 1 with either 0, 3, 5, or 7 wavefront sensors missing at a corner.

For even the best seeing conditions, all the light will be in the halo. Figure 4 shows the short time exposure halo HWHM versus r0. We use the short time exposure HWHM since the guider sensors will operate at 100 Hz. For typical wind speeds, the aperture clearing time is about two seconds. Since the telescope pointing will be corrected very much faster than this, the tilts caused by atmospheric turbulence should be almost completely corrected. Except for impossibly good seeing conditions, the corrected rms spot radii are always much smaller than the turbulence half intensity spot radii for perfect imaging.

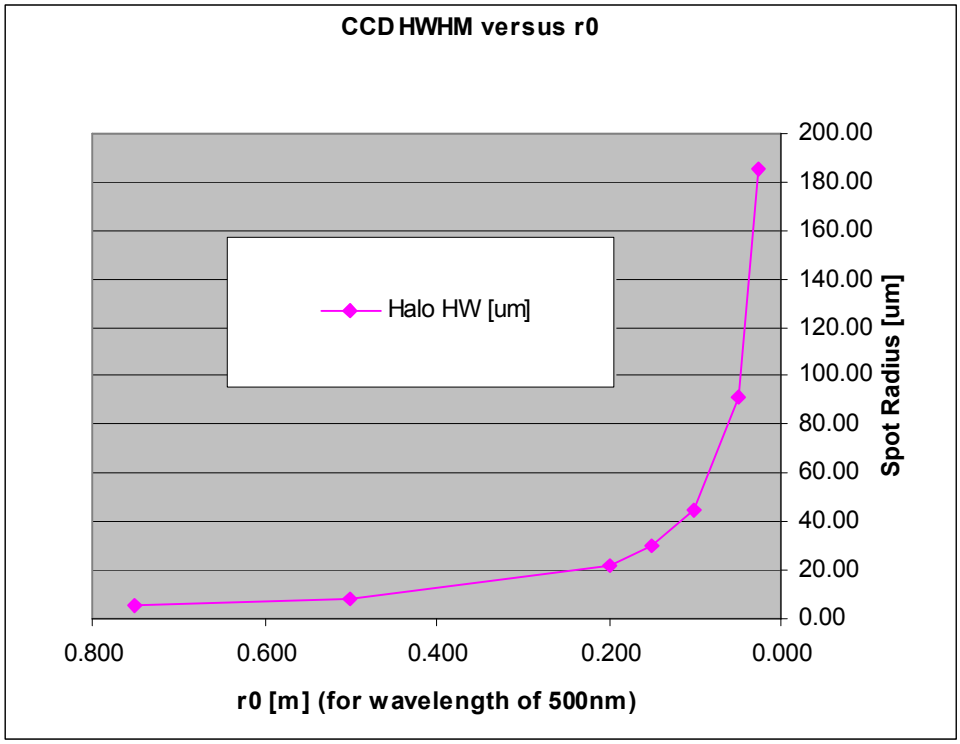

FIGURE 4

Half maximum radius for the spots produced by atmospheric turbulence versus seeing condition assuming the telescope to have perfect imaging.

5. SUMMARY

We have shown that with tomographic wavefront correction the LSST can achieve good imaging across the entire field with at least four wavefront sensors uniformly spaced about the circumference even in rather poor seeing conditions. We have used larger than expected mirror deformations and larger than expected rigid body motions. The SVD least squares algorithm that is used converges in one or two iterations and does not walk off with further iterations. More wavefront sensors on the circumference would substantially improve image quality in poor seeing conditions but in good seeing conditions would give little improvement.

ACKNOWLEDGEMENTS

This research was performed under the auspices of the U.S. Department of Energy by the University of California, Lawrence Livermore National Laboratory under Contract W-7405-ENG-48. The LSST design and development activity is supported by the National Science Foundation under Scientific Program Order No. 9 (AST-0551161) through Cooperative Agreement AST-0132798. Additional funding comes from private donations, in-kind support at Department of Energy laboratories and other LSSTC Institutional Members.

REFERENCES

1. D. W. Sweeney, "Overview of the Large Synoptic Survey Telescope Project", Invited Talk 6267-06, *Astronomical Telescopes and Instrumentation 2006 SPIE Meeting*, Orlando, Florida, May 24-31, 2006.
2. S. S. Olivier, L. G. Seppala, K. Gilmore, L. C. Hale, W. T. Whistler, "LSST camera optics", paper 6273-33, *Astronomical Telescopes and Instrumentation 2006 SPIE Meeting*, Orlando, Florida, May 24-31, 2006.
3. Lynn Seppala, "Optical Design Strategies for the Large-Aperture Synoptic Survey Telescope (LSST)", Invited Talk FWN2, *Optical Society of America 2005 Annual Meeting*, Tucson, Arizona, October 16-20, 2005.
4. Poster Session 26 at the 207th Meeting of the American Astronomical Society, Washington DC, January 8-12, 2006. Available at http://www.lsst.org/Meetings/AAS/Jan2006/jan2006.shtml
5. Chuck Claver, W. J. Gressler, V. L. Krabbendam, S. Olivier, D. Phillion, L. Seppala, R. Upton, LSST "Wavefront Sensing and Alignment System", paper 6273-23, *Astronomical Telescopes and Instrumentation 2006 SPIE Meeting*, Orlando, Florida, May 24-31, 2006.
6. Peter Lancaster and Miron Tismenetsky, *The Theory of Matrices Second Edition* (Academic Press, New York, 1985), 192.
7. William H Press, Saul A Teukolsky, William T. Vetterling, and Brian P. Flannery, *Numerical Recipes in C Second Edition* (Cambridge University Press, Cambridge, 1992), pages 59-70.
8. Regis Tessieres and James H Burge, "Alignment Strategy for the LSST Version 2" (LSST Corporation, June, 2004).
9. *Telescope AO* is written in Visual C++ for Windows XP Professional and can be obtained from phillion1@llnl.gov.
10. D. K. Gilmore, S. M. Kahn, M. Nordby, D. L. Burke, P. O'Connor, J. Oliver, V. Radeka, T. Schalk, R. Schindler, "LSST camera system overview", paper 6269-10, *Astronomical Telescopes and Instrumentation 2006 SPIE Meeting*, Orlando, Florida, May 24-31, 2006.

APPENDIX A COMPUTING THE ADDED TILT DUE TO A TRANSVERSE SHIFT IN THE CLUSTER POINT POSITION

The ABCD ray matrix from the telescope aperture to the image plane has A=0 since any ray parallel to the z axis is imaged to the image plane origin. Consider a parallel ray bundle incident upon the telescope with slope a in the xz plane, where z is the telescope's optical axis. Then:

$$\begin{bmatrix} 0 & B \\ C & D \end{bmatrix} \begin{bmatrix} h \\ \alpha \end{bmatrix} = \begin{bmatrix} B\alpha \\ Ch + D\alpha \end{bmatrix} \tag{A1}$$

This tells us that the transverse image displacement is $\delta x_{cluster} = B\,\alpha$. If we know how α is related to a_2, the coefficient of Zernike x tilt, then we can relate a_2 to the transverse image displacement.z.

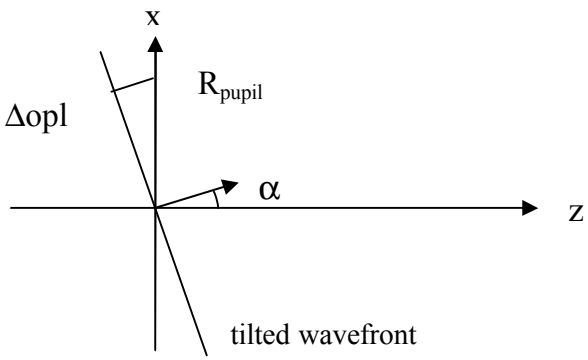

Here $\Delta opl = R_{pupil} \sin(\alpha)$, or, in the small angle approximation, $\Delta opl \approx R_{pupil}\,\alpha$. Now $\Delta opl = a_2\, x / R_{pupil}$. Therefore:

$$a_2 = \frac{R_{pupil}\,\delta x_{cluster}}{B} \tag{A2}$$

APPENDIX B COMPUTING THE ADDED FOCUS DUE TO A LONGITUDINAL SHIFT IN THE CLUSTER POINT POSITION

Suppose the wavefront incident upon the telescope is spherically curved so that we can represent it by a small focus term. Then the total ray matrix is:

$$\begin{bmatrix} 0 & B \\ C & D \end{bmatrix}\begin{bmatrix} 1 & 0 \\ \delta C & 1 \end{bmatrix}=\begin{bmatrix} B\,\delta C & B \\ C+D\,\delta C & D \end{bmatrix} \tag{B1}$$

In image space, the focus is at

$$\delta z_{cluster} = -\frac{B\,\delta C}{C} \tag{B2}$$

A positive $\delta z_{cluster}$ means that the image is beyond the CCD. We wish to obtain an expression for δC in terms of the Zernike focus coefficient a_4. We can then relate a_4 to $\delta z_{cluster}$. Now

$$\delta C = \delta\left(-\frac{1}{f}\right) \tag{B3}$$

The delta opl is given by

$$\Delta opl = a_4\,(2\frac{r^2}{R_{pupil}{}^2}-1) \tag{B4}$$

It is also given by

$$\Delta opl = \frac{r^2}{2}\delta\left(-\frac{1}{f}\right) \tag{B5}$$

Dropping the piston term in Eq (B4) and combining Eq's (B2), (B3), (B4) and (B5), we obtain:

$$a_4 = \left(\frac{-R_{pupil}{}^2\,C}{4\,B}\right)\delta z_{cluster} \tag{B6}$$

APPENDIX C OPTICAL SYSTEM DEFINITIONS IN CODE V FORMAT

The optical system definition is listed completely for the I band. Only the changes are listed for the other bands. Everything is in millimeter units except that the GLASS CODE is the wavelength in nanometers. The CCD, lenses, and, filter comprise an assembly that moves slightly in z whenever the filter is changed. The filter surface 10 on the telescope side always has the same RDY and is always at the same distance from the back surface of the lens before it. The chief rays of the ray bundles for the various field points are normally incident upon this surface. This is the surface which has the bandpass dielectric coating. The filter thickness and the RDY of filter surface 11 on the CCD side vary.

I BAND

```
                RDY             THI       RMD          GLA
  OBJ:        INFINITY        0.000000
    1:        INFINITY        0.000000
    2:        INFINITY        0.000000
  STO:    -19835.00000    -6156.200600    REFL
     ASP:
      K  :   -1.215000
      IC :     YES       CUF:    0.000000
      A  :0.000000e+000   B  :1.381000e-024   C  :0.000000e+000   D  :0.000000e+000

  STO:     -6788.00000     6390.006000    REFL
     ASP:
      K  :   -0.222000
      IC :     YES       CUF:    0.000000
      A  :0.000000e+000   B  :-1.274000e-020   C  :-9.680000e-028   D  :0.000000e+000

  STO:     -8344.50000    -3630.599300    REFL
     ASP:
      K  :    0.155000
      IC :     YES       CUF:    0.000000
      A  :0.000000e+000   B  :-4.500000e-022   C  :-8.150000e-030   D  :0.000000e+000

    6:     -2824.00000      -82.230000            SILICA
    7:     -5021.00000     -412.642020            AIR
    8:        INFINITY      -30.000000            SILICA
  STO:     -2529.00000     -357.580000            AIR
     ASP:
      K  :   -1.570000
      IC :     YES       CUF:    0.000000
      A  :0.000000e+000   B  :1.656000e-018   C  :0.000000e+000   D  :0.000000e+000

   10:     -5624.00000      -15.700000            SILICA
   11:     -5612.00000      -45.300000            AIR
  STO:     -3169.00000      -60.000000            SILICA
     ASP:
      K  :   -0.962000
      IC :     YES       CUF:    0.000000
      A  :0.000000e+000   B  :0.000000e+000   C  :0.000000e+000   D  :0.000000e+000

   13:     13360.00000      -28.500000            AIR
   14:        INFINITY        0.000000
   15:        INFINITY        0.000000
  IMG:        INFINITY        0.000000

REFRACTIVE INDICES
    GLASS CODE                 777.500
    AIR                  1.00000000000
    SILICA               1.45371671941
```

U BAND

	RDY	THI	RMD	GLA
STO:	-8344.50000	-3633.971000	REFL	
10:	-5624.00000	-26.200000		SILICA
11:	-5513.00000	-34.800000		AIR
GLASS CODE		384.000		
SILICA		1.47197937277		

G BAND

	RDY	THI	RMD	GLA
STO:	-8344.50000	-3632.326000	REFL	
10:	-5624.00000	-21.140000		SILICA
11:	-5564.00000	-39.860000		AIR
GLASS CODE		480.000		
SILICA		1.46350217460		

R BAND

	RDY	THI	RMD	GLA
STO:	-8344.50000	-3631.261000	REFL	
10:	-5624.00000	-17.800000		SILICA
11:	-5594.00000	-43.200000		AIR
GLASS CODE		630.000		
SILICA		1.45709968888		

Z BAND

	RDY	THI	RMD	GLA
STO:	-8344.50000	-3630.130000	REFL	
10:	-5624.00000	-14.200000		SILICA
11:	-5624.00000	-46.800000		AIR
GLASS CODE		895.000		
SILICA		1.45182561703		

Y BAND

	RDY	THI	RMD	GLA
STO:	-8344.50000	-3629.915700	REFL	
10:	-5624.00000	-13.500000		SILICA
11:	-5624.00000	-47.500000		AIR
GLASS CODE		987.500		
SILICA		1.45057613775		